

# Faceted wrinkling by contracting a curved boundary

Anshuman S. Pal, Luka Pocivavsek, Thomas A. Witten

*James Franck Institute, Dept. of Physics*

*University of Chicago*

(Dated: June 9, 2022)

Single-mode deformations of two-dimensional materials, such as the *Miura-ori* fold, are important to the design of deployable structures because of their robustness, but usually require careful pre-patterning of the material. Here, we show that inward contraction of a curved boundary produces a novel single-mode deformation without any pre-patterning. Using finite-element simulations of the contraction of a thin circular annular sheet, we show that these sheets wrinkle into a structure with negligible stretching energy, in which the contracted boundary forms spontaneous facets. We construct a strictly isometric wrinkled surface formed of triangles and cones that matches geometric and energy features closely, suggesting that this class of partly-faceted wrinkled deformations is isometric. Isometry favours the restriction of such deformations to a robust low-bending energy channel that avoids stretching. This class of buckling also offers a novel way to manipulate sheet morphology via boundary forces. Finally, it serves as a minimal model for illustrating the strong constraints imposed by geometry in elastic pattern formation.

## I. INTRODUCTION

The flourishing field of extreme mechanics [1–4] seeks ways in which large, spontaneous material deformations yield robust, reproducible structures and motions. Many of these structures exploit the selective deformations shown by thin sheets, which bend or fold easily but resist internal stretching strongly [5–13]. The large resistance to stretching creates strong, non-local constraints that restrict the sheet to selected modes of deformation. A classic example is the *Miura-ori* folding pattern [14–16]. This periodic pattern enables to contract a spread-out flat sheet of paper into a compactly folded state with one single mode of deformation dictated by the pattern (see Fig. 1a). Here we report similar robust deformation of a flat sheet *without* the position-dependent processing of an origami fold. Instead, we specify an initial annular shape and a simple mode of *edge deformation*: contracting the inner boundary radially. The result is a strongly reproducible three-dimensional pattern of high-amplitude wrinkles. We attribute the reproducibility to a qualitative feature of the simulated deformation – it involves virtually no stretching; in the limit of zero thickness, it is “isometric”. This unstretched morphology is made possible by a distinct pattern of flat, triangular facets alternating with smoothly-curving conical segments.

*a.* This paper studies a variant of the classic Lamé radial wrinkling deformation (see Fig. 1b), in which an annular sheet is subjected to uniform tensile forcing at the inner and outer boundaries [17, 19–21]. Our “inner Lamé” variant imposes an inward radial contraction at the inner boundary only. Below, we show how the requirement of isometricity quantitatively accounts for observed features of our simulated inner Lamé annulus, in both its shape and its elastic energy. Specifically, we show that the simulated deformation matches an explicitly isometric deformation of the original annulus into a cone-triangle pattern. We describe the robustness of the structure using a variety of boundary conditions for the contracted inner boundary. We argue that the observed robustness of the cone-triangle structure is a natural consequence of its isometric property. We note how the cone-triangle structure can be induced via different paths, as illustrated in Figs. 1d, e, and f, and discuss generalisations to a broader range of structures.

*b.* Sections II and III define the inner Lamé deformation that we simulate, and the isometric model shape used for comparison. In Section IV, we show that the shape and energy of the simulated sheet are consistent with the model. Finally, Section V addresses our assumptions and discusses the value of such deformations for generating spontaneous structures.

## II. INNER LAMÉ DEFORMATION

Given the circular annulus of Fig. 2a, we define the inner Lamé deformation as the equilibrium shape induced by drawing the inner boundary inward by a distance  $\Delta$ , so that it is forced to live on a cylinder whose radius is reduced by  $\Delta$ . We define the initial inner radius as our unit of length. The pull distance  $\Delta$  thus acts as the sole loading parameter in the system. The system can thus be conveniently defined using only three geometric parameters: thickness  $t$ , the width  $w$ , and displacement ‘loading’  $\Delta$ . The internal forces determining the shape arise from the bending modulus  $B$ , and the in-plane stretching modulus  $Y$ . In thin sheets with thickness  $t$  much smaller than the inner radius and the width  $w$ , the sheet may be taken as virtually unstretchable, and many features of the shape are independent of

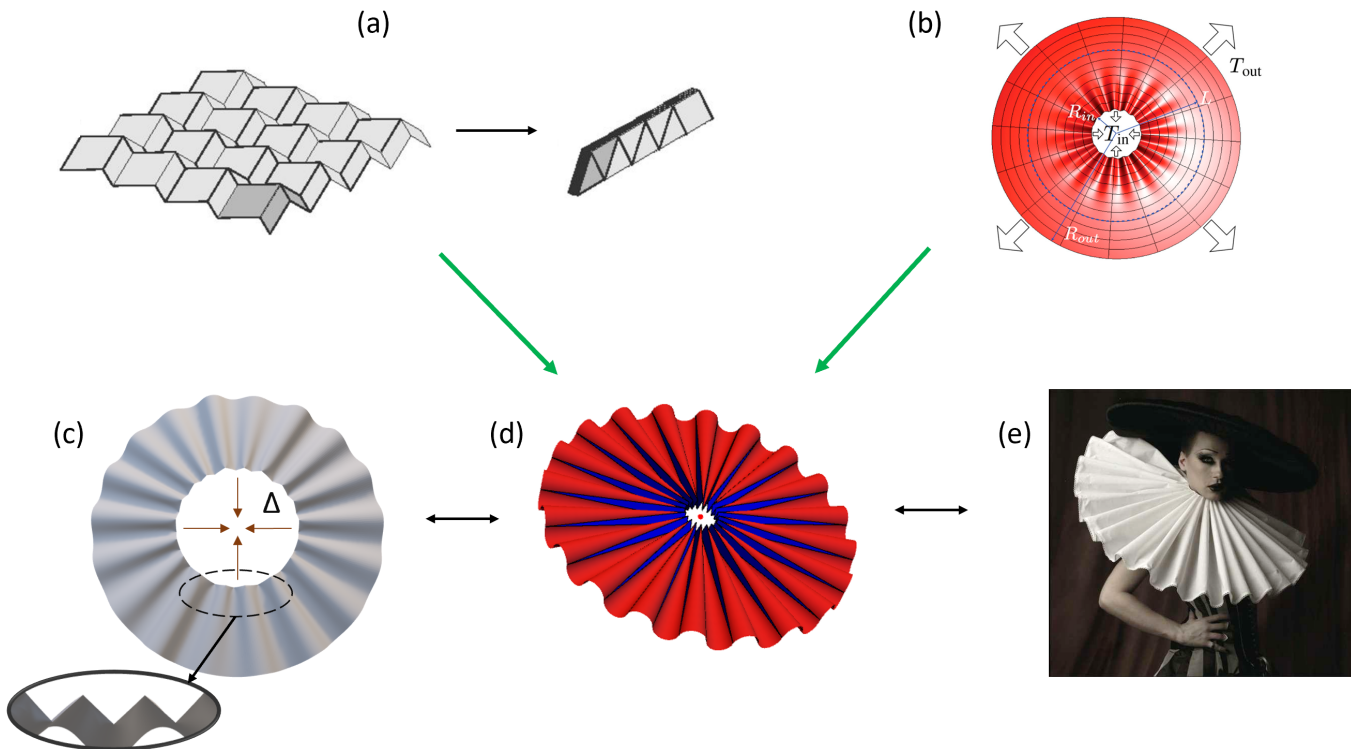


FIG. 1. Geometry-controlled robust radial wrinkling. a) Miura-ori patterns guide a flat sheet to contract into a folded state with a single, continuous motion (adapted from [16]). b) Smooth radial (i.e., Lamé) wrinkling in an annulus under both inner and outer tension, indicated by arrows (adapted from [17]). In this paper, we study Miura-ori like robust deformation of an annulus in a radial Lamé setting. This deformation can be generated in multiple ways. c) Finite-element simulation under uniform radial contraction of the inner boundary, described in *Methods* (inset shows zoom-in of emergent zigzag inner boundary). d) Cone-triangle geometric construction defined in Sec III, with triangles shown in blue and cones in red. e) Ruff collar garment (reproduced from [18]) made by manually pleating the inner boundary of an annular piece of cloth.

Y [17].

*a.* We may anticipate that this inner Lamé deformation is strictly isometric by using the post-buckling far-from-threshold (FT) analysis of ref. [17] for the classic Lamé problem, where tension is applied at *both* the inner and outer boundaries. In the FT regime, the wrinkling slopes grow to the order of unity, and the associated azimuthal stress becomes negligible compared to the pre-buckling stress. Only the *bending stress*, owing to wrinkling and proportional to the bending modulus, remains. The same is expected for our inner Lamé case: consider the radial stress in a narrow sector of the annulus. Equilibrium requires that the net radial force on the sector be zero. In the unbuckled state, the inner tension driving the deformation is balanced by the net outward component of the azimuthal stresses on the sides of the sector. But in the FT regime, this stress is negligible, as argued above. In addition, there is no radial tension at the outer boundary. We conclude that the only forces to balance the inner tension are the weak bending stresses.

*b.* The absence of any deformation stress except for bending stress would imply that the deformed sheet deforms only by bending in the thin limit. That is, it is isometric to the undeformed flat annulus. The limiting shape must thus be ‘developable’ (c.f. Gauss’ *Theorema Egregium*; [22]). This means there must be a *straight* ‘generator’ line through each point of the surface that extends to the boundary without curving in space. In the next sections, we show that the contracted annulus is indeed consistent with a specific developable surface, suggested by the numerically determined shape.

### III. A DEVELOPABLE CONE-TRIANGLE SHAPE

The faceted wrinkling seen in our numerical simulations – made using the commercial software Abaqus (SIMULIA, Dassault Systèmes) – clearly shows the presence of straight directors at the zigzag inner boundary (see Fig. 1c, inset). Moreover, it suggests a further hypothesis: that the wrinkled morphology can be seen as a piecewise union of

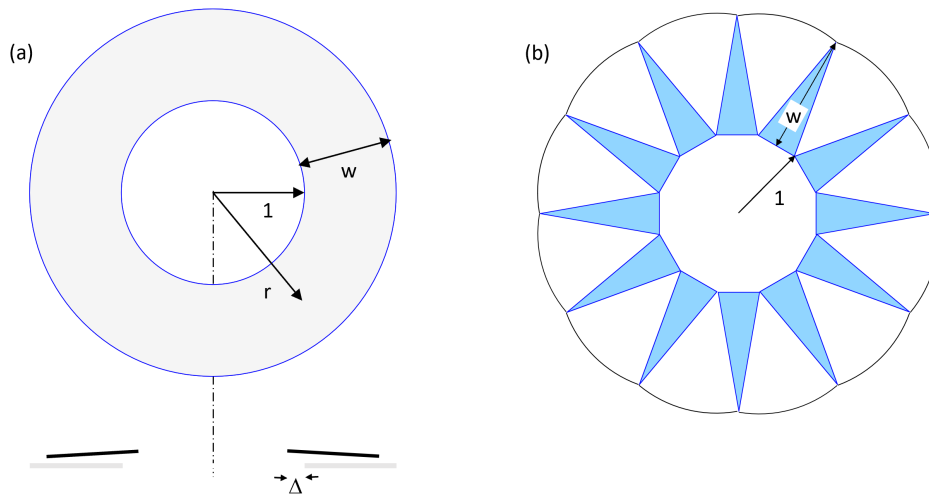


FIG. 2. a) Sketch of the inner Lamé deformation of a horizontal annulus. (Top) Top view showing the undeformed annulus, of inner radius 1 and width  $w$ . (Bottom) Vertical cross-section of the deformed annulus through a line where the vertical displacement of the wrinkle is maximal. The undeformed state is shown in light shading; the dark lines are a section of the deformed annulus, contracted horizontally by a distance  $\Delta$ . These lines are also displaced upward and tilted downward. b) Sketch of the cone-triangle construction in its initial, flat state. Here, we choose wavenumber  $m = 6$ , hence it has 12 triangles (shown in colour). The mid-line and height  $w$  of one triangle are indicated. The white sectors bridging the triangles are shown in white. When the bases of the triangles are moved inward, they must tilt to retain their shape and connectivity. The bridging sectors deform into cones. A typical deformed example is shown in Fig. 1b.

alternating flat triangles and curved cones. We take this as our starting point. For a configuration with wavenumber  $m$ , we consider a flat configuration (see Fig. 2b) where the inner boundary is a  $2m$ -sided polygon. Each segment of this boundary is the base of an isosceles triangle of height  $w$ . To complete the annulus, the apexes of adjacent triangles are joined with an arc. The constructed surface then consists of these triangles and the sectors joining them.

*a.* One may readily specify an isometric deformation that allows the inner boundary of this structure to contract. We deform the initial surface by translating the base of each triangle inward toward the centre, specifying that the triangles remain rigid. In order to maintain their shape and connectivity, the triangles must tilt (i.e. rotate about their mid-lines) increasingly as they are drawn inward; adjacent triangles tilt in opposite directions. The sectors connecting two triangles must then also bend in order to remain connected to their triangles. A ready *isometric* choice for this deformation is to bend the flat sectors into *circular conical arcs*. These arcs need not, however, join smoothly with their adjacent triangles, as further discussed in Sec. IV C.

#### IV. COMPARING SIMULATED DEFORMATION WITH MODEL

In this section, we test whether the isometric/developable cone-triangle construction is able to predict the quantitative features of our simulated inner Lamé deformation from Sec. II. Our commercial Abaqus software uses standard finite-element methods to represent the deformed equilibrium shape as the inner boundary is gradually contracted to move along the axis of the cylinder (as detailed in *Methods*). In comparing this simulation to the cone-triangle construction, we must supply two free parameters: the boundary displacement  $\Delta$ , as well as the wavenumber  $m$ . Thus, we measure the  $\Delta$  and  $m$  of the simulated deformation, and then construct the corresponding geometric solution with the same  $\Delta$  and  $m$ . The first comparison we make is purely qualitative – we superpose the two solutions and observe how well they match up. Fig. 3 shows such a comparison, where we have rotated the geometric solution about the  $z$ -axis to obtain the best superposition. As the figure shows, one may align the two figures so that they overlay well over a significant part of the annulus, with matching zigzags at the inner boundary and matching waves at the outer boundary. Between the inner and outer boundaries, the surfaces match closely enough that the two surfaces alternately hide each other.

*a.* The qualitative resemblance seen in the figure encourages a more quantitative comparison. Accurate comparison is hindered by the variability of the simulated wrinkles. Though regular in general, the wrinkle pattern is not strictly periodic on the annulus. To optimise the comparison, we perturb the initial state of the simulations to promote periodicity. Specifically, we deform the initial state with a low-amplitude, smooth, periodic wrinkle with a

wavelength similar to the original simulations. [23]

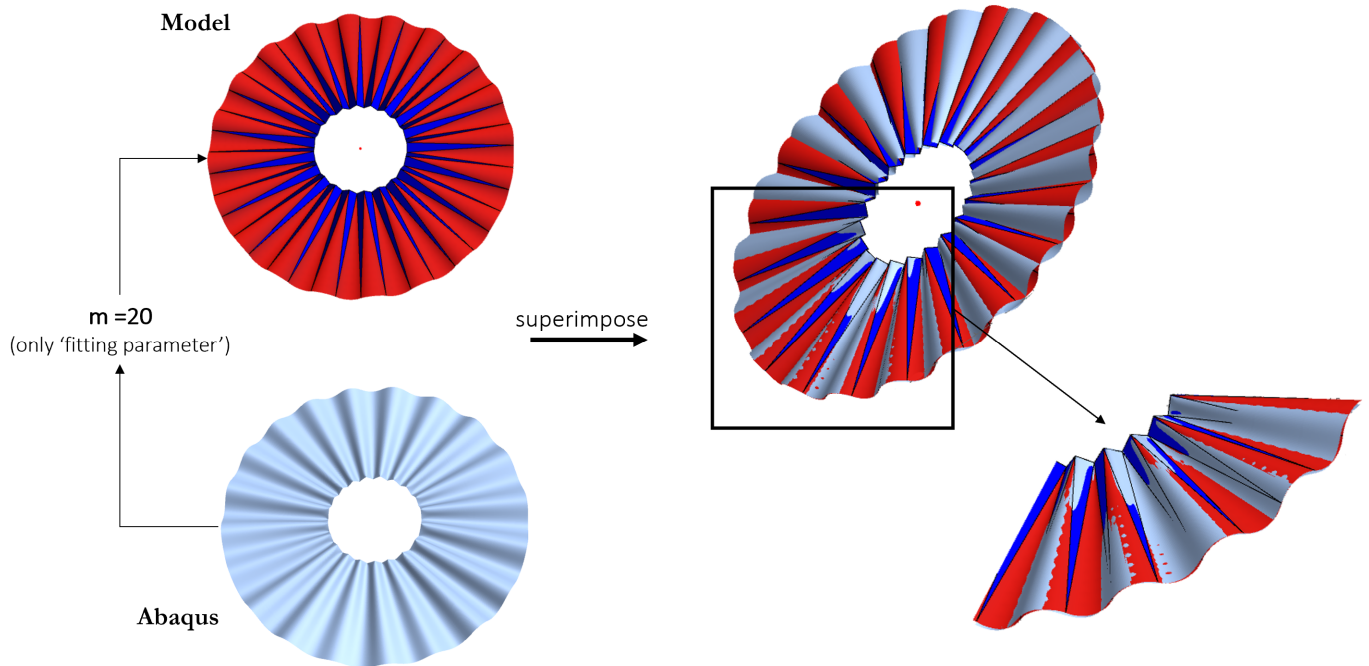


FIG. 3. Qualitative comparison between Abaqus simulation and our cone-triangle model, for a representative sample ( $w = 1.67$ ,  $t = 1.33 \times 10^{-3}$ ). (Left) Given  $w$ ,  $\Delta$  and the wavenumber  $m$  from the Abaqus solution, we construct a model cone-triangle solution (cones in red, triangles in blue) using the procedure described in Section III. (Right) For a qualitative comparison, we superpose the two solutions, with azimuthal rotation as the only degree of freedom. We find close agreement between them; with this top-down view, areas with colour indicate where the model solution is above the Abaqus solution, while those in grey indicate the opposite. In particular, the zoomed-in boxed portion shows close matching at both inner and outer boundaries. Zooming out to the whole annulus, we see that there is a ‘phase mismatch’ between the two solutions, with part of the solution in-phase (the boxed region) and part of it out-of-phase. This is due to the non-uniform size of the wrinkles in the Abaqus solution.

### A. Inextensibility and bending strains

We first verify the anticipated isometry of the sheet as announced in the *Introduction*. To this end, we consider a material circle at radius  $r$  in the annulus; its arc length  $L(r)$  is necessarily  $2\pi r$ , and independent of the displacement  $\Delta$ . However, since the position of this circle is displaced inward by an amount  $\Delta$ , the horizontal projection of the circle has a length  $L_{xy}(r) = 2\pi(r - \Delta)$  [24]. Thus the relative change in  $L_{xy}$  on deformation is given by

$$(L_{xy} - L)/L = -\Delta/r. \quad (1)$$

The “contraction factor”  $\Delta/r \equiv \tilde{\Delta}(r)$  is useful for the comparisons below.

*a.* We test the validity of 1 by explicitly measuring  $L_{xy}$  for the inner and outer boundary circles in the simulation. In the simulation, these boundaries consist of a sequence of straight segments, one for each finite element. We add up the segment lengths and their  $xy$  planar projections to obtain  $L_{xy}/L$  as a function of  $\Delta$ . Fig. 4b shows representative data testing Eq. 1 at both inner ( $r = 1$ ) and outer ( $r = 1 + w$ ) boundaries. The data points (left side of Eq. 1) seem to line up perfectly with the linear prediction (right side of Eq. 1). However, closer inspection shows a tiny deviation between two two. This is because Eq. 1 requires exact isometry, whereas the simulation cannot be an exact isometry due to its non-zero thickness. The difference  $L_{xy}/L - 1 + \tilde{\Delta}$  between prediction and data in Eq. 1 is thus caused by a residual azimuthal strain, which we denote  $\epsilon_{\theta\theta}^{\text{resid}}$ . At the inner boundary, this strain is caused by *localised* stretching at the cone tips, and can thus be neglected. At the outer boundary, however, this strain should result from the isometric *bending stress* described in Section II; measuring it thus provides a further test of isometry.

b. We know that *Elastica* bending at scale  $\lambda$  induces a residual bending stress,  $\sigma_{\theta\theta}^{\text{resid}} \sim B/\lambda^2$ , where  $B$  is the bending modulus. Thus, for wrinkling of wavenumber  $m$ , we expect the outer boundary to have an azimuthal bending strain given by:

$$\epsilon_{\theta\theta}^{\text{resid}} \sim \frac{1}{Y} \frac{B}{\lambda^2} \sim \frac{m^2 t^2}{(1+w)^2}, \quad (2)$$

where we have used  $\lambda = 2\pi(1+w)/m$  and  $B/Y \sim t^2$  ( $t$  is the thickness). The inset of Fig. 4b is a log-log plot of  $\epsilon_{\theta\theta}^{\text{resid}}$  versus  $\frac{m^2 t^2}{(1+w)^2}$ , at fixed  $\Delta$ , for multiple samples with differing values of  $m$ ,  $t$  and  $w$ . We get data collapse over the range of a decade, with the predicted slope of unity. Thus, Fig. 4b provides strong evidence for inextensibility of the numerical solutions at both boundaries.

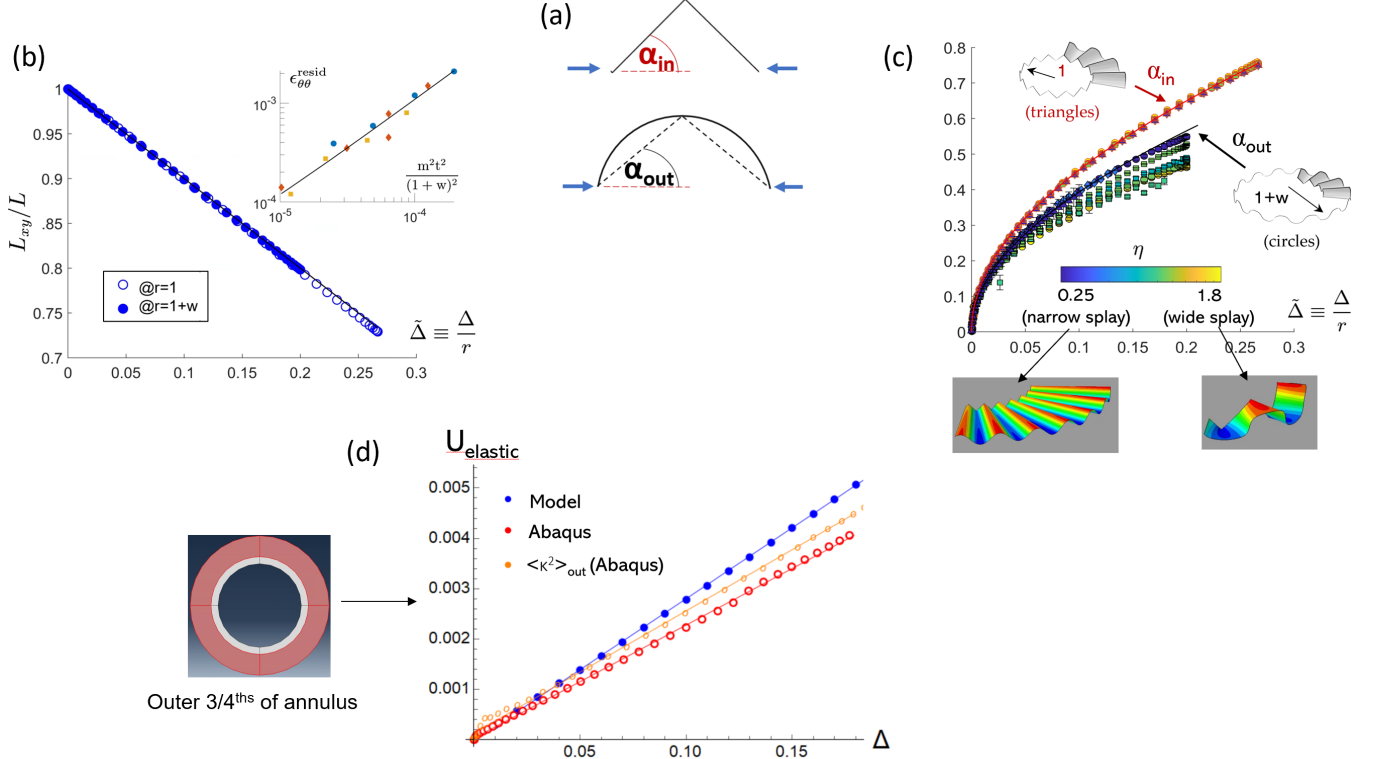


FIG. 4. Quantitative comparisons between theory and Abaqus simulations (using the explicitly periodic simulations described at the beginning of Sec. IV). (a) Sketches of the wrinkle profile at the inner ( $r = 1$ ) and outer ( $r = 1 + w$ ) boundaries, showing the definition of slope angles  $\alpha_{\text{in}}$  and  $\alpha_{\text{out}}$ . (b) Testing inextensibility at inner and outer boundaries (see Sec. IV A). The main graph shows a typical example of testing Eq. 1 (for  $w = 0.33$ ,  $m = 10$ ,  $t = 1.33 \times 10^{-3}$ ); Abaqus data points capture the left side of the equation while the black theory line is the right side. (inset) The residual strain at  $r = 1 + w$ ,  $\epsilon_{\theta\theta}^{\text{resid}} \equiv L_{xy}/L - 1 + \tilde{\Delta}(1+w)$ , plotted logarithmically against the bending strain  $m^2 t^2 / (1+w)^2$  at fixed  $\Delta$ , for different values of  $m$ ,  $t$  and  $w$  (see Eq. (2)). Legend:  $w = 0.33$  (blue circles),  $w = 0.67$  (red diamonds),  $w = 1.0$  (yellow squares). The black line shows the linear fit:  $\epsilon_{\theta\theta}^{\text{resid}} = 10.8 \frac{m^2 t^2}{(1+w)^2} + 10^{-5}$ . (c) Comparing wrinkle slope angle vs. applied contraction  $\tilde{\Delta}$  (see Sec. IV B). (Top row) We separately test Eq. (3) for  $\alpha_{\text{in}}$  (in red) and Eq. (4) for  $\alpha_{\text{out}}$  (in black). The Abaqus data points are plotted alongside the model predictions. Abaqus samples of differing width  $w$  and wavenumber  $m$  are coloured using the dimensionless cone splay parameter,  $\eta \equiv \frac{\pi(1+w)}{mw}$ . The error bars are standard deviations from averaging over all the wrinkles. Markers:  $w = 0.33$  (circles),  $w = 0.67$  (squares),  $w = 1.0$  (diamonds),  $w = 1.67$  (triangles). (Bottom row) Example wrinkle profiles for small and large  $\eta$ : (left) for  $\eta = 0.25$  ( $w = 1.0$ ,  $m = 25$ ), and (right) for  $\eta = 1.8$  ( $w = 0.33$ ,  $m = 7$ ). Colouring denotes height. (d) Comparing elastic energies (see Sec. IV C):  $U_{\text{elastic}}^{\text{Abaqus}}(\Delta)$  (in red) with  $U_{\text{elastic}}^{\text{model}}(\Delta)$  (in blue) and  $U_{\langle\kappa^2\rangle}^{\text{Abaqus}}(\Delta)$  (in yellow). (Left) Annulus, indicating the region where energies were compared (in red), omitting the high-curvature regions near  $r = 1$ . (Right) We plot the results for a representative sample ( $w = 1.0$ ,  $m = 25$ ,  $t = 6.67 \times 10^{-4}$ ). All three curves show *Elastica*-like linear scaling (solid lines are fits), but the two theoretical curves overestimate the Abaqus energy by roughly 15% and 30%. Other  $w$  and  $m$  values also generally over-estimated the energies, as discussed in Sec. IV C.

## B. Evolution of wrinkle amplitude

We now compare specific features of the wrinkle shape to the predictions of the cone-triangle construction. In Fig. 4c, we consider the amplitude of the observed wrinkles. We measure this amplitude by determining the average slope angle  $\alpha$  of the wrinkles at the inner and outer boundaries. Though the cone-triangle construction can be implemented for a wide range of wavenumbers  $m$  for any given  $\Delta$  and  $w$ , we considered only the narrow range of  $m$  that appeared spontaneously in the unbiased Abaqus simulations. In practice, these had roughly  $7 \leq m \leq 35$ .

*a.* We define the average slope angle  $\alpha$  to be the slope angle of the line joining the zero-crossing of the wrinkle with the adjacent maximum (illustrated in Fig. 4a). For angle  $\alpha_{\text{in}}$  at the inner boundary, the figure explicitly relates  $\alpha_{\text{in}}$  to  $L_{xy}/L$ . Using Eq. 1, we have:

$$\cos \alpha_{\text{in}} = 1 - \Delta \equiv 1 - \tilde{\Delta}(1). \quad (3)$$

At the outer edge,  $L_{xy}/L$  is the ratio of the horizontal line to the arc length of the circular sector in Fig. 4a. For our circular cone model, it is related to the slope angle  $\alpha_{\text{out}}$  by

$$\sin 2\alpha_{\text{out}}/(2\alpha_{\text{out}}) = L_{xy}/L \equiv 1 - \tilde{\Delta}(1+w). \quad (4)$$

In Fig. 4c, we compare these cone-triangle slope angles to the simulated ones as a function of  $\tilde{\Delta}(r)$  for both inner ( $r = 1$ ) and outer ( $r = 1 + w$ ) boundaries. The upper red curve and data points compare  $\alpha_{\text{in}}$ . The agreement of the data points with the curve confirms that each triangle segment tilts to preserve its length as it is drawn towards the axis. The solid black curve gives the cone-triangle prediction of Eq. 4 for  $\alpha_{\text{out}}$ . The data points on and beneath the curve represent annuli of different widths  $w$  and wavenumber  $m$ , coloured by their splay:  $\eta \equiv \pi(1+w)/(mw)$ . In general, our circular cone model is consistent with the prediction for narrowly-splayed wrinkles, but over-estimates the slopes for widely-splayed ones. The pictures below the graph show the annulus shape for different amounts of splay  $\eta$ . They suggest the source of the over-estimated slopes: for the widely splayed example with the greatest discrepancy, the boundary curve is significantly flatter than a circular arc. Thus the simplifying assumptions of our triangle-cone construction are not satisfied in this widely-splayed regime.

## C. Comparing energies

Perhaps the main significance of this isometric deformation is that its energy behaves so differently from that of a generically deformed sheet. It is different in two respects. Firstly, the energy depends only on the bending modulus  $B$ , and is independent of the stretching modulus  $Y$  for given bending modulus. Secondly, the energy in this limit is qualitatively smaller than for a generic deformation with comparable curvature and thickness. Below we verify that the energy of the contracted annulus has these distinctive features.

*a.* The elastic energy is a sum of strain energy and bending energy:

$$U_{\text{elastic}} = U_{\text{strain}} + U_{\text{bend}}$$

Thus, for a strain-free isometric configuration, we have  $U_{\text{elastic}} \approx U_{\text{bend}}$ . For a conical deformation extending between  $L_{\text{min}}$  and  $L_{\text{max}}$  – as measured along the cone axis – the bending energy is given by:

$$U_{\text{bend}}^{\text{cone}} = \frac{B}{2} \log\left(\frac{L_{\text{max}}}{L_{\text{min}}}\right) \int ds \kappa^2, \quad (5)$$

where  $\kappa(s)$  is the normal curvature of the outermost arc of the cone, parameterised by the arc length  $s$ . For a circular cone as in our model,  $\kappa(s) = \text{const.} = 1/\rho_c$ , where  $\rho_c$  is the radius of the outermost circle. Then, adding up the contribution of  $2m$  cones for a wrinkled solution of wavenumber  $m$  (see SI for details), we get:

$$U_{\text{elastic}}^{\text{model}}(\Delta) = U_{\text{bend}}^{\text{model}}(\Delta) \approx B \log\left(\frac{L_{\text{max}}}{L_{\text{min}}}\right) \frac{\pi(1+w)w}{\rho_c^2(\Delta)}, \quad (6)$$

where the approximation is for large- $m$  solutions. Here, the bending modulus  $B = \frac{Et^3}{12(1-\nu^2)}$  (with  $E$  the Young's modulus,  $\nu$  the Poisson ratio, and  $t$  the thickness) can be calculated directly from the material properties of the Abaqus solution. Also, in order to avoid high-curvature regions near  $r = 1$  where the thin-sheet approximation  $\kappa t \ll 1$  becomes questionable, we choose to compare energies for only the outer  $3/4^{\text{th}}$  part of the annulus, so that  $\log(\frac{L_{\text{max}}}{L_{\text{min}}}) = \log(4)$ .

b. In Eq. (6), the only dynamic variable is  $\rho_c(\Delta)$ . Our circular cone construction (see SI) permits us to get an expression for  $\rho_c(\Delta)$  in terms of the outer slope angle  $\alpha_{\text{out}}$ :

$$\rho_c(\Delta) \approx \frac{\pi(1+w)}{4m} \frac{1}{\alpha_{\text{out}}(\Delta)}. \quad (7)$$

We recall that  $\alpha_{\text{out}}$  depends only on  $w$  and  $\Delta$ , and not on  $m$ . Thus  $\rho_c \sim 1/m$ , and so  $U_{\text{elastic}}^{\text{model}} \sim m^2$ , which is the quadratic scaling with wavenumber (at fixed amplitude) expected for a bending energy.

c. Our primary subject of interest, however, is the scaling of  $U_{\text{elastic}}^{\text{model}}$  with  $\Delta$  for fixed  $m$ . Since  $\alpha_{\text{out}}(\Delta) \sim \sqrt{\Delta}$  approximately (see Fig. 4c), we expect the squared curvature and the bending energy to scale linearly with  $\Delta$ :  $U_{\text{elastic}}^{\text{model}} \sim 1/\rho_c^2 \sim \Delta$ . We note that this linear form is the same as for the *Elastica* energy of a rod under weak Euler buckling [25], which is expected since each transverse arc of the cone undergoes Euler buckling with this same  $\Delta$  dependence.

d. In Fig. 4d, we plot three energy curves for a typical sample. These curves compare the simulated energy for a typical example,  $U_{\text{elastic}}^{\text{Abaqus}}(\Delta)$  (in red), with two theoretical estimates:  $U_{\text{elastic}}^{\text{model}}(\Delta)$  (in blue; see Eq. 6) calculated from our cone-triangle model, and  $U_{\langle \kappa^2 \rangle}^{\text{Abaqus}}(\Delta)$  (in yellow) calculated indirectly from the Abaqus solution through measurement of the mean squared curvature at the outer boundary:  $\langle \kappa^2 \rangle_{\text{out}} \equiv \frac{1}{2\pi(1+w)} \int ds \kappa^2$ , and by using Eq. 5. We see that the two theoretical estimates are larger than the simulation energy by a constant factor of order unity. This pattern was seen in all our simulations. The extra energy seen from the circular-cone model (blue curve) is a consequence of that very approximation – our circular cones are constructed to fit into the narrowed sector angle of the contracted sheet without compressing or stretching. However, the actual bent sectors must satisfy a further condition, even in the asymptotic limit of zero strain, viz. continuity of the first derivative. Thus, each sector must meet the adjacent flat triangle smoothly, with no change in the normal vector. In the regime we studied, the slope-angle at the cone-triangle boundary is too large to match the adjacent triangle, giving excess bending energy in the cone. The observed discrepancy in this slope is compatible with the discrepancy in bending energy.

e. The  $U_{\langle \kappa^2 \rangle}^{\text{Abaqus}}(\Delta)$  curve infers the conical bending energy using the (non-constant) observed surface curvature at the simulated outer boundary. The observed curvature was smaller than the circular arc at the cone-triangle boundary and greater at the mid-line. This estimate gave an energy much closer than the simulated energy, but still not in agreement with it. This indicates that the surface is not of the assumed conical shape throughout the curved surface measured. The surface could attain a smaller energy while matching the outer boundary shape if its directors did not converge to a point but instead converged more weakly. We have not settled whether this remaining discrepancy is owing to a) discretisation error in the simulation, or b) a residual effect of nonzero sheet thickness, which would become smaller with decreasing thickness.

f. We conclude that the elastic energy of deformation for the wrinkles encountered in this study is strongly consistent with our claim of an isometric conical deformation, with the accuracy increasing for narrow wrinkles (having small parameter  $\eta$ ). Furthermore, the explicit cone-triangle construction gives a workable quantitative estimate of the full elastic energy, provided we supply the observed wrinkle wavenumber  $m$ .

## V. DISCUSSION

### A. A developable wrinkling morphology

As shown above, our variant of the Lamé radial contraction system is qualitatively altered by removing the outer tension from that system. The mechanics in our system is governed instead by the constraints of isometric deformation, dictating a developable surface in the limit of zero thickness. While developability has been hypothesised and used as tool to study buckling in several contexts [26–29], in our favourable case, we have been able to account for all the details of the structure with a simple periodic cone-triangle ansatz.

a. To the best of our knowledge, such reconstruction of a wrinkled configuration through fundamental developable building blocks is novel in the field of thin sheet elasticity. That an *a priori* complicated wrinkled surface can be broken down into such a two-part *macroscopic* unit cell is indicative of the strong geometric simplifications brought about by developability and Gauss' *Theorema Egregium*. Furthermore, unlike previously-known faceted structures – which are composed of only flat facets [30–32] – faceted wrinkling has both flat triangles and curved cones. This cone-triangle decomposition also provides an instructive example of a buckled shape in a radially symmetric system that does not have the conventional separable form – i.e. the buckling displacement is not a product of a radial factor and azimuthal factor.

*b.* The developability of the faceted wrinkling structure makes it fundamentally geometric, so that it can be created easily on a computer. This provides a way to programmatically construct *smooth* radially wrinkled patterns in materials using intrinsically flat components, much in the spirit of origami and other designed materials [4]. In fact, a well-known real world example of such programmed radial wrinkling is the Elizabethan ruff collar. One way of making a ruff is exactly using the inner Lamé boundary conditions: we take a cloth annulus, and manually make pleats in it such that the inner boundary of the annulus lives on a contracted radius. Figs. 1e and 1d show, resp., a ruff collar and its reconstruction using our cone-triangle model; the visual similarity between the two is striking. The conical outer solution seems to perfectly capture the ruff wrinkles, in particular their radial straightness and their shape at the outer boundary.

## B. Wavelength selection

As is clear from the ruff example, the faceting and developability discussed in this paper is completely independent of the number of wrinkles (viz. the wavenumber  $m$ ). That is because these features are set independently. Wavelength determination is controlled by the minimisation of the bending energy, whereas we are concerned in this paper almost entirely by the minimisation of the strain energy. This is in keeping with the standard paradigm of understanding wrinkled morphologies in thin sheets [17], where separation of energy scales means that the gross features of the morphology are determined by minimising the dominant strain energy, while the finer features (like wavelength) are controlled by the sub-dominant bending energy. Wavenumber determination will be discussed in a future paper. For now, we note that  $m$  seems to grow without bound as the sheet becomes thinner, as in the tensile classical Lamé case. Yet the reason must be entirely different, since the tensile case is governed by non-bending work, which is absent in the present system.

## C. Assumptions

### 1. Circular cone ansatz

The key modelling assumption used in this paper is the circular ansatz for the bent cones. As we have shown, this ansatz serves as a good approximation to the true energy-minimising *Elastica* solution, while being simple enough to allow for explicit calculation of several key observables, viz. the slope  $\alpha_{\text{out}}$  and the energy  $U_{\text{elastic}}$ . Sec. IV shows that this approximation is accurate only for relatively narrow cones (small  $\eta$ ) and large  $w$ . This can be partially explained as follows. We expect the circular ansatz to hold true only for *weak* Euler buckling. ‘Weak’ here means that the applied contraction, and the resultant slope, are both small. In the SI, we show that the contraction experienced by a conical sector increases sharply with decreasing  $w$ , such that for our narrowest annuli, the contraction can be as high as 15 – 20%. At such large values, one no longer expects the weak Euler regime to be valid, and the resultant shape manifests its non-linearity through the flattening apparent in Fig. 4c. We note, however, that even at such large contractions, both the circular ansatz and the numerical simulations give a linear energy profile, although their slopes are no longer close.

### 2. Inner boundary approximation

In the physical problem of Sec. II, the inner boundary is constrained to lie on a cylinder. Our cone-triangle surface clearly does not satisfy this condition exactly; its inner boundary consists of straight lines, and does not match the cylindrical surface exactly. Instead, the cone-triangle surface solves a closely related problem in which the cylinder is replaced by a polygonal cylinder with  $2m$  vertical facets. For the thin sheets we studied numerically, the number of wrinkles  $m$  grows without bound for very thin sheets, so that the mismatch between the real cylinder and the faceted cylinder becomes arbitrarily small. In the numerical samples, we looked for strains along the inner boundary owing to this inner boundary approximation. We detected no change in the length of the inner zigzag line as the contraction  $\Delta$  increases.

*a.* Still, the inexactness of the triangle construction at the inner surface makes it clear that the construction is not a realistic representation of a circular annulus contracted onto a cylinder for *arbitrary* wavenumber  $m$ . Likewise, we have no evidence that an annulus constrained to have a given small  $m$  remains developable under contraction. Our only evidence for this developable shape applies to the range of  $m$  that the system spontaneously chooses, or larger.

### 3. Lateral constraint boundary condition

A further remark concerns the boundary conditions used in our Abaqus simulations. As noted in *Methods*, we prohibit any lateral movement of the nodes on the inner boundary, in order to stabilise the faceted wrinkled regime against folding instabilities. However, if we do allow lateral movement, we see the same faceted wrinkling *at early times*, before azimuthal movement of the boundary quickly leads to folding instabilities. This suggests that faceting can be seen for weak buckling, even in the absence of lateral constraints. But our evidence is still only suggestive and needs to be confirmed through physical experiments.

#### D. Role of thickness

The role of the thickness  $t$  (or its absence) in our work also merits some attention. Our developable cone-triangle construction lives in the asymptotic zero-thickness limit, and thus thicker sheets might be expected to deviate from it significantly. However, our analytical construction accurately models the wrinkled morphology for even moderately thick sheets (our thickest simulated sheet had  $t = 2.67 \times 10^{-2}$ ). In fact, the example of the ruff collar (Fig. 1e) suggests that the cone-triangle asymptotic solution is valid practically even for macroscopically thick sheets. This suggests that deviations from our asymptotic solution are restricted to the localised boundary layers of stress in the otherwise isometric solution – the areas of so-called ‘stress concentration’ [30]. These are zones where the radius of curvature becomes comparable to the thickness, leading to divergent bending energy density. To prevent this, such zones are ‘smoothed out’ at the cost of some localised strain; in our wrinkled solution, we see such point-like boundary layers at the tips of the cones. These boundary layers are expected to shrink to zero radius as a sheet approaches the zero-thickness limit. However, since such boundary layers are localised and have negligible effect on the overall solution (see SI), we did not investigate them any further in the present study.

#### E. Generalisation

Can our model be generalised? The key modification applied in this paper to the traditional Lamé problem is the freeing up of the outer boundary. This allows the radial tension in the sheet to vanish, and also allows the outer boundary to deform freely. In the absence of any tension or other non-elastic sources of work [33, 34], and following our reasoning, we should see analogous faceted wrinkling with any contraction of the inner curved boundary of a sheet. The isosceles triangles and right-circular cones associated with the axisymmetric Lamé geometry will have to be correspondingly generalised to arbitrarily shaped triangles and cones, but the rest should follow as described in this paper. Separately, one can also imagine attaching the inner boundary to a constraining cone instead of a cylinder. This will impose an angle instead of a displacement at the inner boundary, thereby breaking the up-down symmetry of Lamé wrinkling. Thus, our work can act as a starting point for analysing an entire class of boundary-controlled wrinkling morphologies, whose prototype is an annulus contracted at its inner boundary.

#### F. Application

The deformation geometry treated here amounts to a strategy for avoiding the typical fate of deformed sheets. Such sheets adopt structures that require significant elastic energy beyond the needed bending energy. Often these structures produce uncontrolled disorder, e.g. , as seen in a crumpled sheet. By contrast, the radial contraction used here guides the sheet into a low-energy channel resulting in only bending energy. This low-energy state is moreover attainable by continuous deformation from a flat reference state. Since these deformations lack the additional deformation costs of competing structures, they are intrinsically stable. They provide a general means to fold and compact a sheet continuously and reversibly with minimal external guidance. We note that the curved inner boundary appears important in stabilising this structure; straight boundaries with no radial contraction [9] do not produce analogous regular wrinkling.

#### G. Conclusion

While the emergence of developability in wrinkled systems has been studied intensively over the past decade, the simplicity and symmetry of the Lamé geometry makes it a particularly clean realisation of such a phenomenon. In

fact, the inner Lamé system may be considered a direct 2d equivalent to the prototypical 1d Euler *Elastica* system. Both cases consider pure bending of a system whose stretching energy has been set to zero. The faceted, developable morphology of the Lamé case in particular highlights the strong geometric constraints entailed by isometry in 2d. This faceted morphology is qualitatively different from previously known forms of 2d wrinkling. Significantly, it creates sharply dictated, strongly distorted features without stretching and without a separable radial/azimuthal shape. Moreover, it has many variants to be explored, with real world applications. There remain also fundamental mysteries like the wavelength selection to be explained; this problem will be the focus of future work.

## VI. ACKNOWLEDGEMENTS

The authors would like to thank Benny Davidovitch, Dominic Vella and Enrique Cerda for many insightful discussions, and Nhung Nguyen and George Papazafeiropoulos for help with numerical analysis. This work was partially funded by the National Science Foundation (NSF)-Materials Research Science and Engineering Center (MRSEC) grants DMR-1420709 and DMR-2011854.

## VII. SI: CONSTRUCTION OF CIRCULAR CONICAL SECTIONS

In the main text, we describe how we divide the flat annulus into two regions – an inner region composed of isosceles triangles, and an outer region composed of arc sectors. The main text describes how the inner triangles can isometrically deform under an inner displacement (or contraction) of length  $\Delta$  by tilting about the normal to the inner boundary – this gives an inner ‘buckled’ solution. Here, we describe how to construct the outer solution whereby the arc sectors isometrically bend into sections of right-circular cones. In other words, each arc bends into a circular profile.

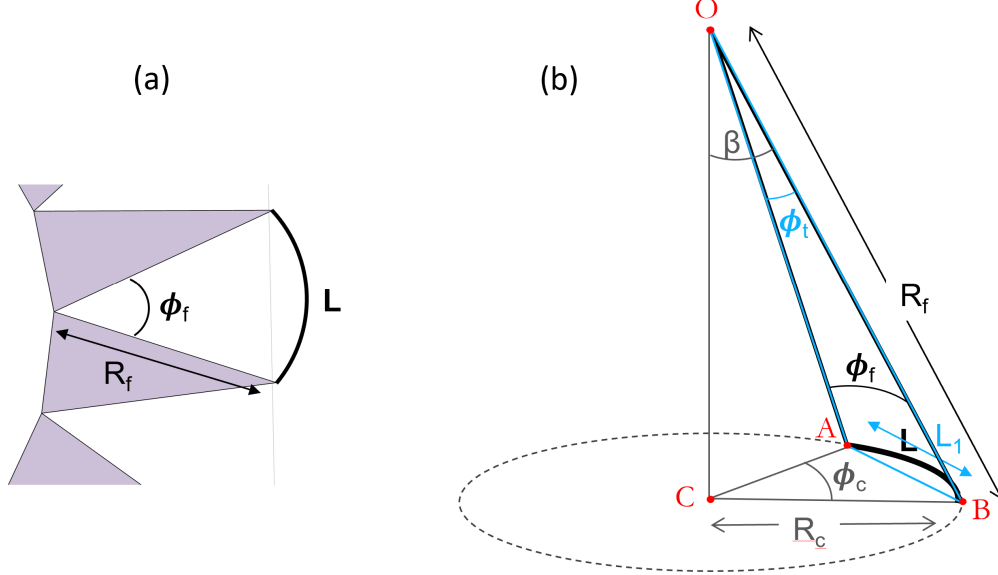


FIG. 5. Isometrically constructing a sector of a cone from a flat arc sector. (a) The flat configuration. (b) The curved configuration; the actual conical sector and its variables are depicted in black, the triangle  $\triangle AOB$  formed by the edges of the two adjacent tilted triangles, along with its variables, is in blue, and the putative cone with its variables is in grey.

*a.* The requisite variables for our geometric construction are described in Fig. 5. In the flat state, each arc sector, lying between two adjacent flat triangles, subtends an angle  $\phi_f$  at the common vertex of these two triangles. If the edges of the triangles have length  $R_f$ , then the length of the largest arc is  $L = R_f\phi_f$ . On tilting, the edges of these same triangles approach each other, so that they subtend a reduced angle  $\phi_t$  (see SI Fig. 6a). This reduction in angle ( $\Delta\phi = \phi_t - \phi_f \leq 0$ ) constitutes the effective compressive strain  $\epsilon_{\text{cone}} = \Delta\phi/\phi_f$  for the arc sector. SI Fig. 6a shows the evolution of  $\epsilon_{\text{cone}}$  with boundary contraction  $\Delta$ . We see clearly that narrower sheets feel a greater  $\epsilon_{\text{cone}}$  for the same  $\Delta$ .

*b.* The excess material can be accommodated by bending the sector into a cone. The exact shape of this cone can be determined by solving the *Elastica* equation with the appropriate boundary conditions. However, for simplicity, in this paper we choose to approximate the exact shape by a circular cone. The aim then is to find the circular cone that fits in between the two adjacent triangles while exactly accommodating the excess angle  $\Delta\phi$ . Fig. 5b shows all the variables needed for this operation. The isometrically bent conical section has to fit inside the triangle  $\triangle AOB$  (drawn in teal) defined by the apex 0 and the tilted edges  $OA$  and  $OB$  (see also Fig. 3 in main text). The conical section itself is drawn in bold black. Let the circular cone have angular extent  $\phi_c$ , and let its maximum radius be  $\rho_c$ , centred at point  $C$ . Then the conical shape can be determined from the following set of geometric constraints.

*c.* The first constraint is that of inextensibility, i.e. length conservation. This gives us:

$$L = \rho_c\phi_c = R_f\phi_f. \quad (8)$$

The second constraint involves specifying the end-to-end distance  $L_1$  between points A and B. Thus, using the blue triangle  $\triangle AOB$  and the grey triangle  $\triangle ACB$  in Fig. 5b, we have:

$$L_1 = 2\rho_c \sin(\phi_c/2) = 2R_f \sin(\phi_t/2). \quad (9)$$

Eqns. (8) and (9) constitute a set of simultaneous equations for the cone variables  $\rho_c$  and  $\phi_c$ , since  $R_f$  and  $\phi_f$  are fixed by the flat geometry, while  $\phi_t$  is set by the tilt of the neighbouring angles. Finally, using basic trigonometry, we

have for the cone's apex angle:

$$\sin \beta = \rho_c / R_f. \quad (10)$$

In sum, we have three independent equations for three unknowns:  $\phi_c$ ,  $\rho_c$  and  $\beta$  (all positive-definite), which fully specify the cone in space (including the centre  $C$ ). SI Fig. 6b shows a representative solution of such a constructed cone. SI Fig. 6c shows the evolution of this construction with increasing  $\Delta$ .

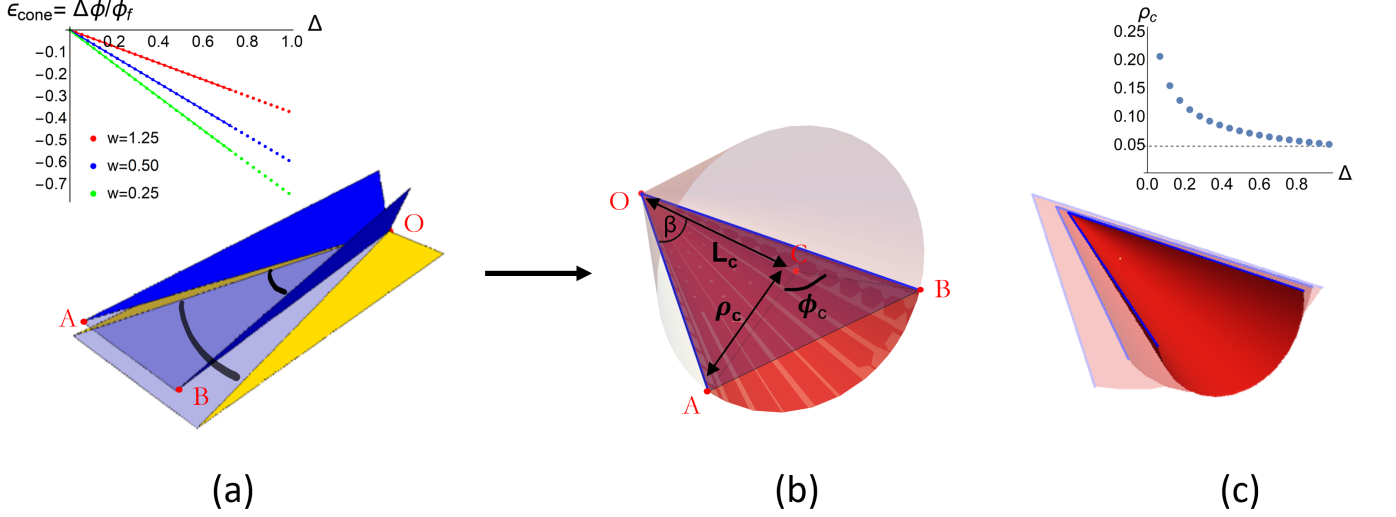


FIG. 6. Constructing a single cone (see Sec. III and SI for details). (a) Two adjacent flat triangles (in yellow) subtending an angle  $\phi_f$ , on tilting (in deep blue), subtend a smaller angle  $\phi_t$ . Thus, the region between the triangles (shown approximately as a violet triangle) gets *squeezed* by an angle  $\Delta\phi = \phi_t - \phi_f$ . (inset) Evolution of the conical strain  $\epsilon_{\text{cone}} = \Delta\phi/\phi_f$  with  $\Delta$  for three different widths  $w$ . Model measurements are plotted alongside the predicted lines of slope  $= -1/(1+w)$ . (b) To fit within the contracted boundary defined by  $OA$  and  $OB$ , the region must bend into a circular cone of radius  $\rho_c$ , angular extent  $\phi_c$ , axial length  $L_c$  and tilt angle  $\beta$ . The only ingredients needed for the construction are  $\triangle AOB$  and the contraction  $\Delta$ . (c) The evolution of the conical solution with  $\Delta$  (here,  $0.05 \leq \Delta \leq 0.6$ ). Greater opacity means larger  $\Delta$ ; the cones are translated with respect to each other for viewing clarity. (inset) As  $\Delta$  increases, the radius of curvature  $\rho_c$  decreases, and for  $\Delta \rightarrow 1$ , attains an asymptotic value of  $\rho_c \approx \frac{\pi w}{2m}$  (dotted line).

### A. Correcting for scalloped arc sectors

The flat arc sectors as defined above – circular arcs with their origin at the inner boundary – lead to the creation of a flat shape that is in fact a *scalloped* annulus, whose outer circumference  $2mR_f\phi_f$  is greater than the expected  $2\pi(1+w)$ .

We can correct for this length discrepancy when constructing the bent cones, by changing  $R_f \rightarrow \chi R_f$  in Eq. (8) where  $\chi = \frac{\pi(1+w)}{mR_f\phi_f} \leq 1$ . Eq. (9) remains unchanged since it specifies the end-to-end-distance, which is set by the neighbouring tilted triangles. We note that this factor  $\chi$  is smallest for samples with small  $w$  and  $m$  (wide splay  $\eta$ ), and becomes  $\approx 1$  for large  $w$  and  $m$  (narrow splay).

### B. Limits of the cone-triangle construction

To the best of our knowledge, the above conical construction works as long as the initial (flat) angle  $\phi_f < \pi$ , i.e. as long as the edges of two adjacent triangles define a triangle. The value of  $\phi_f$  depends on the width  $w$  and the wavenumber  $m$ , and increases as  $m$  decreases. This defines a minimum wavenumber  $m_{\text{min}}^{\text{cone}}(w)$  below which a conical solution is invalid. For a sufficiently wide annulus, we find that  $m_{\text{min}}^{\text{cone}} = 2$ , which is the minimum possible value for *any* wrinkled solution. However, for very narrow annuli, this value goes up. Thus, for  $w = 0.2$ , we find  $m_{\text{min}}^{\text{cone}} = 4$ . Fig. 7 shows two such contrasting geometries.  $m_{\text{min}}^{\text{cone}}(w)$  defines a geometric limit beyond which we expect

our cone-triangle model to fail. However, the main text shows that we already see significant deviations from our model for Abaqus solutions with wavenumber  $m$  significantly higher than  $m_{\min}^{\text{cone}}(w)$ .

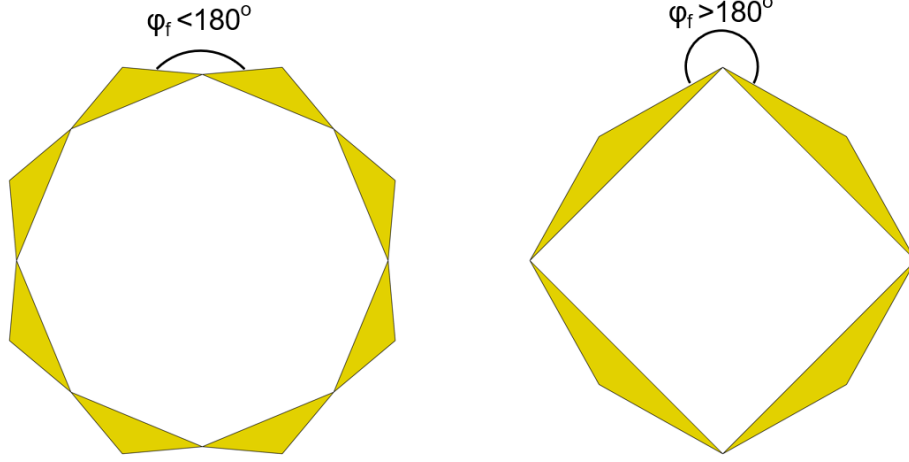


FIG. 7. Two different flat state geometries for  $w = 0.2$ . (Left) For  $m = 4$ , the flat angle  $\phi_f < \pi$ , which allows the conical construction described in Sec. VII B. (Right) For  $m = 2$ , the flat angle  $\phi_f > \pi$ , which means that our conical construction is not valid here.

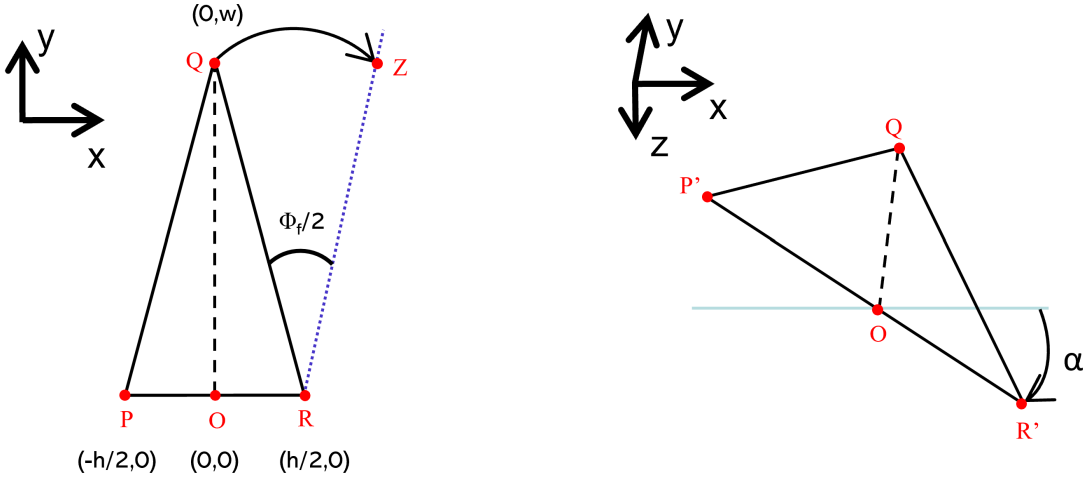


FIG. 8. Diagram describing the geometric problem for determining  $\phi_t$ . (Left) Top view of the flat isosceles triangle  $\triangle PQR$  lying in the x-y plane, having height  $w$  and base  $h$ .  $OQ$  is the perpendicular bisector of  $PR$ .  $\phi_f$  is the angle between  $QR$  and the dotted (vertical) blue plane. (Right) End view of the same triangle rotated clockwise by angle  $\alpha$  about the y-axis.

### VIII. SI: CALCULATING THE CONICAL STRAIN $\epsilon_{\text{cone}}(\Delta)$

Fig. 6a shows the evolution of the conical strain  $\epsilon_{\text{cone}}$  with contraction  $\Delta$ . The observations (plotted with dots) show that  $\epsilon_{\text{cone}}(\Delta)$  is linear, with the slope depending significantly on the width  $w$  of the sheet, but independent of the wavenumber  $m$ . To understand this behaviour, we analytically derive an expression for  $\epsilon_{\text{cone}}(\Delta) = (\phi_t - \phi_f)/\phi_f$ .

*a.* Since  $\phi_f$  is fixed, to find  $\epsilon_{\text{cone}}$ , we only need to calculate  $\phi_t(\Delta)$ . The angle  $\phi_t(\Delta)$  can be calculated given any one of the inner triangles, the flat arc angle  $\phi_f$ , and the tilt angle  $\alpha$ . The geometric problem is defined in Fig. 8. Here,  $\phi_t$  is the angle between the rotated vector  $\overrightarrow{QR'}$  and the vertical blue plane defined by  $\overrightarrow{RZ}$ . Also,  $w$  is the annular width, and  $h = \pi/m$ . Then our steps are as follows:

1. Find the 3-vector  $\overrightarrow{OR'} = \mathbb{R}_{-\alpha} \cdot \overrightarrow{OR}$ , where  $\mathbb{R}_{-\alpha}$  is the 2x2 rotation matrix of angle  $\alpha$  about the y-axis (viz.  $\overrightarrow{OQ}$ ).
2. Then  $\overrightarrow{R'Q} = \overrightarrow{OQ} - \overrightarrow{OR'} = (-h/2 \cos \alpha, w, h/2 \sin \alpha)$ .
3. We only need its orthogonal projection on to the x-y plane: the 2-vector  $\overrightarrow{R'Q}_{\perp} = (-h/2 \cos \alpha, w)$ .
4. We need the vector angle between this and the vertical blue plane defined by  $\overrightarrow{RZ}$ . Here,  $\overrightarrow{RZ} = \mathbb{R}_{-\phi_f/2} \cdot \overrightarrow{RQ}$ , where  $\overrightarrow{RQ} = (-h/2, w)$ .

Finally, we have  $\phi_t = 2\text{VectorAngle}[\overrightarrow{R'Q}_{\perp}, \overrightarrow{RZ}]$ . The final expression is complex and composed of trigonometric functions. But using  $\cos \alpha = 1 - \Delta$  (recall that the inner radius = 1), and expanding to linear order in  $\Delta$ , we have:

$$\Delta\phi \equiv \phi_t - \phi_f \approx -\frac{h/w}{(h/2w)^2 + 1} \Delta + \dots, \quad (11)$$

where  $h/w = \frac{\pi}{mw} \ll 1$  for most of our samples. Finally, we also have  $\phi_f \approx \frac{\pi(1+w)}{mw}$ , where  $1+w$  is the outer radius. Therefore, we get for the dimensionless conical contraction:

$$\epsilon_{\text{cone}} \equiv \frac{\Delta\phi}{\phi_f} \approx \frac{h}{w\phi_f} \Delta \approx -\frac{1}{1+w} \Delta. \quad (12)$$

The prediction of Eq. 12 is plotted alongside measurements in the inset of SI Fig. 6a. The two are fully consistent. This explains why wider cones should feel less contraction for a given  $\Delta$ .

## IX. SI: CALCULATING BENDING ENERGY FOR A CONE

In this section, we continue with the variables introduced in section SI-I. A right-circular cone is made up of a series of circles whose radii  $\rho$  increase linearly with distance (say,  $z$ ) along the cone axis, measured from the cone tip. For a cone of axial length  $L_c$  (see SI Fig. 6a) and maximum radius  $\rho_c$ , we thus have:  $\rho(z) = \frac{\rho_c}{L_c} z$ . We can also write  $\frac{\rho_c}{L_c} = \tan \beta$ , where  $\beta$  is the cone's vertex angle.

*a.* Now, an infinitesimally wide circular band of radius  $\rho$ , angular extent  $\phi_c$ , and width  $\frac{dz}{\cos \beta}$ , has bending energy  $= B \frac{1}{\rho^2} \times (\phi_c \rho) \times \frac{dz}{\cos \beta}$ , where  $B$  is the bending modulus. Integrating over an entire conical sector, we get:

$$U_{\text{bend}}^{\text{cone}} = B \frac{\phi_c}{\cos \beta} \int_0^{L_c} dz \frac{1}{\rho(z)} \quad (13)$$

$$= B \phi_c \frac{1}{\cos \beta \tan \beta} \int_0^{L_c} \frac{dz}{z} \quad (14)$$

Any physical cone must have a *finite* bending energy, and thus must depart from the conical shape near  $z = 0$ . Thus, the conical shape can only be realistic beyond a minimum axial distance  $L_{\text{core}}$ . For this outer region, the energy becomes:

$$U_{\text{bend}}^{\text{cone}} = B \frac{\phi_c}{\sin \beta} \log\left(\frac{L_c}{L_{\text{core}}}\right), \quad (15)$$

where  $\beta = \tan^{-1} \frac{\rho_c}{L_c}$ . For small angle  $\beta$  (i.e. large  $\Delta$ ), Eq. (15) can be simplified to:

$$U_{\text{bend}}^{\text{cone}} \approx B \phi_c \frac{L_c}{\rho_c} \log\left(\frac{L_c}{L_{\text{core}}}\right), \quad (16)$$

Here,  $\phi_c$ ,  $\rho_c$  and  $L_c$  are all functions of the contraction  $\Delta$ . But  $\phi_c$  and  $\rho_c$  are related through the constraint:  $\phi_c \rho_c = L = \frac{\pi(1+w)}{m}$  (see Eq. 8), and  $L_c \approx w$  (the width of the annulus), so  $U_{\text{bend}}^{\text{cone}}$  can be reduced to a function of the single variable  $\rho_c$ . For the entire annulus, we need to multiply this by the wavenumber  $m$ . Thus, we get:

$$U_{\text{bend}}^{\text{theory}} \approx B \frac{\pi(1+w)w}{\rho_c^2} \log\left(\frac{w}{L_{\text{core}}}\right), \quad (17)$$

More generally, for a cone extending between axial limits  $L_{\text{min}}$  and  $L_{\text{max}}$ , we have:

$$U_{\text{bend}}^{\text{theory}}(\Delta) \approx B \frac{\pi(1+w)w}{\rho_c^2(\Delta)} \log\left(\frac{L_{\text{max}}}{L_{\text{min}}}\right), \quad (18)$$

This is the expression given in the main text.

b. While Eqs. (17) and (18) seem independent of  $m$ , it is not so. Eq. (7) in the main text shows that  $\rho_c \sim (1+w)/m \implies U_{\text{bend}}^{\text{theory}} \sim m^2$ , as expected of a bending energy. We note that this  $\rho_c \sim 1/m$  scaling could have been predicted in another way. In the limit of maximum contraction ( $\Delta \rightarrow 1$ ), the point C approaches the xy-plane, and so the diameters of the  $2m$  circles must approximately equal the reduced projected outer perimeter:  $2\pi(1+w-\Delta) \rightarrow 2\pi w$ . This gives us:  $4m\rho_c \rightarrow 2\pi w \implies \rho_c \rightarrow \frac{\pi w}{2m}$  (the dotted line in the inset of SI Fig. 6c). Indeed, even if C is off the x-y plane (e.g. for smaller  $\Delta$ ), the diameters of the  $2m$  circles must still equal the reduced perimeter  $2\pi(1+w-\Delta)$  up to some factor. Thus, we have the scaling relation  $\rho_c \sim 1/m$  as expected.

c. Finally, we note that the data presented in the paper represents the full expression 15, without any approximation.

## X. SI: ESTIMATING THE STRAIN ENERGY CONCENTRATED AT THE CONE TIPS

The elastic energy of an isometric system is given purely by the bending energy:  $U_{\text{elastic}} = U_{\text{bend}}$ . However, as mentioned in the main text, the isometric solution is not valid at the tips of the conical sections located on the inner boundary. The expected divergence in bending energy at these points is regularised by localised stretching - the so-called zones of stress (or strain) concentration (see [30]). In some systems (e.g. [28, 35, 36]), such concentrated stress energy is found to be comparable to the bending energy  $U_{\text{bend}}$ . While section IV C (alongside Fig.4d) of the main text convincingly argues that the elastic energy of our isometric annulus is given entirely by the bending energy, we would nevertheless like to independently verify that the strain energy localised at cone tips is negligible compared to  $U_{\text{bend}}$ .

a. For this, we estimate the strain energy concentrated at the cone tips. For a single cone tip, this is given by  $U_{\text{strain}} \sim Y\epsilon_{\text{core}}^2 R_{\text{core}}^2$ , where  $Y = Et$  is the stretching modulus ( $E$  is the Young's modulus and  $t$  the thickness),  $R_{\text{core}}$  is the approximate size of the strain localisation zone (the 'core region'), and  $\epsilon_{\text{core}}$  is the localised strain. Through measurements of the stress and strain from the Abaqus samples, we estimate  $\epsilon_{\text{core}} \sim 10^{-3}$  and  $R_{\text{core}} \sim 10^{-2}$  (compare to system size of roughly 1). Furthermore, we find that these two variables are independent of system size, and only depend (weakly) on the thickness  $t$ . To estimate  $U_{\text{strain}}$ , we consider two thicknesses. For the thinner case,  $t = 1 \times 10^{-4}$ , we have  $Y \sim 100$ ,  $\epsilon_{\text{core}} \sim 10^{-3}$  and  $R_{\text{core}} \sim 10^{-2}$ . This gives  $U_{\text{strain}} \sim 10^{-8}$ , which is entirely negligible with respect to the bending energy ( $U_{\text{bend}} \sim 10^{-4} - 10^{-3}$ ). Again, for  $t = 1 \times 10^{-3}$ , we have  $Y \sim 1000$ ,  $\epsilon_{\text{core}} \sim 5 \times 10^{-3}$  and  $R_{\text{core}} \sim 10^{-2}$ , giving  $U_{\text{strain}} \sim 10^{-6}$ , which is again negligible before the bending energy.

## XI. SI: FEA SIMULATION METHODS

For our simulations, we used the commercial finite-element software Abaqus 2018 (Simulia, Dassault-Systemes, Providence, RI). We employed both the dynamic explicit and dynamic implicit methods in the quasi-static limit; 'dynamic' means that the solution is found by forward integration of the equations of motion, while 'explicit' and 'implicit' refer to the integration scheme (resp. they correspond to variations of forward and backward Euler integration). The mixture of these two methods was done partly as a consistency check, partly for convenience, and partly by necessity. While the implicit method in the quasi-static limit was faster for most jobs, the explicit solver was indispensable for the thinnest samples ( $t = 2 \times 10^{-4}, 1 \times 10^{-4}$ ), where the static solver ran into convergence problems. Ensuring the quasi-static limit is also easier for dynamic implicit than for explicit. In dynamic implicit, the quasi-static option is in-built, but for dynamic explicit, it has to be ensured manually by applying the loading slowly enough so that the ratio of kinetic to strain energy stays strictly below 10%. For the thinnest samples, e.g. this involved applying the contraction  $\Delta$  over a time period  $T = 120$  (system units). As a result, the slowest simulations, for the thinnest and widest sheets, lasted  $\approx 30$  hours with 4 cores; the average simulation however, lasted between 2-8 hours on 4 cores.

a. The assembly consisted of only a single annulus, with inner radius fixed and taken to be unity, and with varying width  $w$  and thickness  $t$  in order to test the geometric Lamé system over a wide range of system parameters. For width, we used values  $w = 0.20, 0.33, 0.67, 1.0, 1.67$  (a factor of roughly 10, ranging from very narrow to moderately wide), and for thickness, we used values  $t = 2.67 \times 10^{-3}, 1.33 \times 10^{-3}, 6.67 \times 10^{-4}, 2.67 \times 10^{-4}, 1.33 \times 10^{-4}$  (a factor of 20, ranging from moderately thick to very thin). While the thickness varies over a decade, the values still fall well within the thin sheet limit. The annular part was made of 2d shell quad (S4R) elements. This choice was made mainly to optimise speed, since we used a very fine mesh to ensure that the results be independent of meshing. For comparison, the coarsest mesh we used was for the  $w = 1.67$  annulus, with 60 elements across the radius and 1400 elements across a circle, giving a maximum linear size for an element  $\approx 0.008$ . For consistency checks however, we also ran some simulations with annuli made of 3d cubic (C3D8R) elements (which run far more slowly).

*b.* For the material properties, we used a neo-Hookean hyperelastic model, with coefficients  $C_{10} = 1.5375 \times 10^5$ ,  $D_1 = 3.2520 \times 10^{-7}$ . These coefficients are related to the more well-known linear elasticity moduli by the relations:  $C_{10} = G/2$  (where  $G$  is the shear modulus), and  $D_1 = 2/K$  (where  $K$  is the material bulk modulus). The corresponding Poisson ratio is given by  $\nu = \frac{3/(C_{10}D_1)-2}{6/(C_{10}D_1)+2} = 0.475$ . The choice of modulus (and Poisson ratio) was made to optimise computational performance for the dynamic explicit simulations, since the material modulus affects the wave speed and hence the stable time increment within a dynamic formulation. Too soft a modulus makes it difficult to attain the quasi-static limit, while a very large modulus or perfect incompressibility ( $\nu \rightarrow 0.5$ ) leads to divergence in the stable time increment and very long simulation times. For the implicit method, the choice of modulus is not so important.

*c.* To generate wrinkling, we applied ‘ $\theta$ -fixed’ boundary conditions at the inner boundary:  $u_r(r = 1) = -\Delta$ ,  $u_\theta(r = 1) = 0$ , while keeping the outer boundary at  $r = 1 + w$  free. We usually used  $\Delta \leq 0.267$ . However, applying such an in-plane loading to a planar sheet is not enough to generate buckling automatically. To do so, we need to first perturb the flat state with a small imperfection; for this, we first solved the linear stability prob in Abaqus with  $z$ -pinned BC at  $r = 1$ :  $u_r(r = 1) = -\Delta$ ,  $u_\theta(r = 1) = 0$ ,  $u_z(r = 1) = 0$ , and then used a small amplitude combination of calculated eigenmodes as a perturbation. This is standard procedure for doing post-buckling analysis in Abaqus.

---

- 
- [1] K. Krieger, Extreme mechanics: Buckling down, *Nature* **488**, 146 (2012).
- [2] K. Bertoldi, V. Vitelli, J. Christensen, and M. van Hecke, Flexible mechanical metamaterials, *Nature Reviews Materials* **2**, 10.1038/natrevmats.2017.66 (2017).
- [3] C. D. Santangelo, Extreme mechanics: Self-folding origami, *Annual Review of Condensed Matter Physics* **8**, 165 (2017).
- [4] S. J. Callens and A. A. Zadpoor, From flat sheets to curved geometries: Origami and kirigami approaches, *Materials Today* **21**, 241 (2018).
- [5] E. Cerda and L. Mahadevan, Geometry and Physics of Wrinkling, *Physical Review Letters* **90**, 074302 (2003).
- [6] E. Cerda, L. Mahadevan, and J. M. Pasini, The elements of draping, *Proceedings of the National Academy of Sciences* **101**, 1806 (2004).
- [7] T. Mora and A. Boudaoud, Buckling of swelling gels, *Eur. Phys. J. E* **20**, 119 (2006).
- [8] Y. Klein, E. Efrati, and E. Sharon, Shaping of elastic sheets by prescription of non-euclidean metrics, *Science* **315**, 1116 (2007).
- [9] H. Vandeparre, M. Piñeirua, F. Brau, B. Roman, J. Bico, C. Gay, W. Bao, C. N. Lau, P. M. Reis, and P. Damman, Wrinkling Hierarchy in Constrained Thin Sheets from Suspended Graphene to Curtains, *Physical Review Letters* **106**, 224301 (2011).
- [10] J. Hure, B. Roman, and J. Bico, Stamping and wrinkling of elastic plates, *Physical Review Letters* **109**, 054302 (2012).
- [11] D. Vella, J. Huang, N. Menon, T. P. Russell, and B. Davidovitch, Indentation of Ultrathin Elastic Films and the Emergence of Asymptotic Isometry, *Physical Review Letters* **114**, 014301 (2015).
- [12] B. Davidovitch, Y. Sun, and G. M. Grason, Geometrically incompatible confinement of solids, *Proceedings of the National Academy of Sciences* **116**, 1483 (2019).
- [13] J. D. Paulsen, Wrapping liquids, solids, and gases in thin sheets, *Annual Review of Condensed Matter Physics* **10**, 431 (2019).
- [14] K. MIURA, Method of packaging and deployment of large membranes in space, The Institute of Space and Astronautical Science report , 1 (1985).
- [15] L. Mahadevan and S. Rica, Self-organized origami, *Science* **307**, 1740 (2005).
- [16] M. Schenk and S. D. Guest, Geometry of miura-folded metamaterials, *Proceedings of the National Academy of Sciences* **110**, 3276 (2013).
- [17] B. Davidovitch, R. D. Schroll, D. Vella, M. Adda-Bedia, and E. A. Cerda, Prototypical model for tensional wrinkling in thin sheets, *Proceedings of the National Academy of Sciences* **108**, 18227 (2011).
- [18] Kristian schuller photography, <https://www.trendhunter.com/trends/hdr-photography>.
- [19] J. Huang, M. Juskiewicz, W. H. de Jeu, E. Cerda, T. Emrick, N. Menon, and T. P. Russell, Capillary wrinkling of floating thin polymer films, *Science* **317**, 650 (2007).
- [20] M. Piñeirua, N. Tanaka, B. Roman, and J. Bico, Capillary buckling of a floating annulus, *Soft Matter* **9**, 10985 (2013).
- [21] J. D. Paulsen, V. Démery, K. B. Toga, Z. Qiu, T. P. Russell, B. Davidovitch, and N. Menon, Geometry-Driven Folding of a Floating Annular Sheet, *Physical Review Letters* **118**, 048004 (2017).
- [22] M. P. do Carmo, *Differential Geometry of Curves & Surfaces* (Prentice Hall, 1976).
- [23] The initial wrinkle shape chosen is an eigenmode obtained from linear stability analysis performed in Abaqus.
- [24] Here we treat the radial lines in the material as nearly horizontal, as they are for large wavenumber  $m$ .
- [25] B. Audoly and Y. Pomeau, *Elasticity and geometry* (OUP Oxford, 2010).
- [26] E. Cerda and L. Mahadevan, Conical Surfaces and Crescent Singularities in Crumpled Sheets, *Physical Review Letters* **80**, 2358 (1998).
- [27] M. Ben Amar and Y. Pomeau, Crumpled paper, *Proceedings of the Royal Society of London. Series A: Mathematical, Physical and Engineering Sciences* **453**, 729 (1997).
- [28] A. Lobkovsky, S. Gentges, H. Li, D. Morse, and T. A. Witten, Scaling Properties of Stretching Ridges in a Crumpled Elastic Sheet, *Science* **270**, 1482 (1995).
- [29] M. A. Dias, L. H. Dudte, L. Mahadevan, and C. D. Santangelo, Geometric Mechanics of Curved Crease Origami, *Physical Review Letters* **109**, 114301 (2012).
- [30] T. A. Witten, Stress focusing in elastic sheets, *Reviews of Modern Physics* **79**, 643 (2007).
- [31] K. A. Seffen and S. V. Stott, Surface texturing through cylinder buckling, *Journal of Applied Mechanics* **81**, 10.1115/1.4026331 (2014).
- [32] H. Pham Dinh, V. Démery, B. Davidovitch, F. Brau, and P. Damman, From Cylindrical to Stretching Ridges and Wrinkles in Twisted Ribbons, *Physical Review Letters* **117**, 104301 (2016).
- [33] J. Huang, B. Davidovitch, C. D. Santangelo, T. P. Russell, and N. Menon, Smooth Cascade of Wrinkles at the Edge of a Floating Elastic Film, *Physical Review Letters* **105**, 038302 (2010).
- [34] J. D. Paulsen, E. Hohlfeld, H. King, J. Huang, Z. Qiu, T. P. Russell, N. Menon, D. Vella, and B. Davidovitch, Curvature-induced stiffness and the spatial variation of wavelength in wrinkled sheets, *Proceedings of the National Academy of Sciences* **113**, 1144 (2016).
- [35] J. Kim, J. A. Hanna, R. C. Hayward, and C. D. Santangelo, Thermally responsive rolling of thin gel strips with discrete variations in swelling, *Soft Matter* **8**, 2375 (2012).
- [36] J. Kim, J. A. Hanna, M. Byun, C. D. Santangelo, and R. C. Hayward, Designing responsive buckled surfaces by halftone gel lithography, *Science* **335**, 1201 (2012).